Liu *et al. Cancer Nanotechnology* (2022) 13:11
https://doi.org/10.1186/s12645-022-00117-y

Cancer Nanotechnology

RESEARCH Open Access

New anti-tumor strategy based on acid-triggered self-destructive and near-infrared laser light responses of nano-biocatalysts integrating starvation–chemo–photothermal therapies

Kanglin Liu[1†], Shaoying Yan[2†], Zhengshu Liu[3†], Dan Wang[1,4], Qing Yang[4], Xinyun Jiang[1], Liuxian Chen[1] and Hua Tang[1*]

[†]Kanglin Liu, Shaoying Yan and Zhengshu Liu equally contributed to this work.

*Correspondence: tanghua86162003@cqmu.edu.cn

[1] Key Laboratory of Molecular Biology for Infectious Diseases (Ministry of Education), Institute for Viral Hepatitis, Department of Infectious Diseases, The Second Affiliated Hospital, Chongqing Medical University, 1 Yi Xue Yuan Road, Chongqing 400016, China
Full list of author information is available at the end of the article

Abstract

Background: Inherent limitations of single cancer therapy are overcome by multi-therapy modality, which integrates characteristics of each therapeutic modality and material chemistry. The multi-modal method has the potential for becoming one of the next generation options for cancer treatments. Photothermal therapy (PTT) is an efficient, non-invasive treatment method that can be used on various cancer types. We propose an acid-triggered self-destructing nano-biocatalyst integrated starvation/chemical/photothermal triple therapy that is based on design principles and biomedical applications of GOx cancer treatment methods.

Methods: Scanning electron microscopy (SEM), transmission electron microscopy (TEM), dynamic light scattering (DLS), and zeta potentials were used to analyze the physical as well as chemical properties of MoS_2@DOX/GOx@MnO_2 (M@D/G@M). Further, Fourier transform infra-red (FTIR), X-ray photoelectron spectroscopy (XPS), and X-ray diffraction (XRD) were used to assess the compositions of the nanocatalysts. The biological effects of M@D/G@M on cells were studied in vitro by inverted fluorescence microscopy, confocal laser scanning microscopy (CLSM), flow cytometry, CCK-8 test, and hemolysis test. Treatment effects of the nanocatalysts were evaluated in MHCC-97H tumor BALB/c mice, whose body weights, tumor local temperature, tumor volumes, and tumor histological changes were evaluated.

Results: There was a high DOX encapsulation efficiency of M@D/G@M (90.233%). The photothermal conversion efficiency (η) of M@D/G@M is 25.2%, and its oxygen production within 5 min reached 27.5 mg L^{-1}. Cell internalization analysis showed that within 4 h, M@D/G@M was almost completely absorbed by HepG2 cells. Further, the highest red fluorescence and apoptosis effects of dead cells (59.07% apoptosis) as well as the lowest tumor volume index of mice (0.2862%) were observed in the M@D/G@M + pH6.0 + NIR treatment group.

Conclusions: Our findings inform the development and applications of multi-modal methods in tumor therapy.

Keywords: Nanocatalysts, Glucose oxidase, Starvation therapy, Near-infrared laser (NIR) irradiation, Tumor therapy

Introduction

Globally, cancer is among the leading causes of morbidity and mortality. An estimated 19.3 million new cancer cases (18.1 million excluding non-melanoma skin cancer) and 10.0 million cancer deaths (9.9 million excluding non-melanoma skin cancers) occurred in 2020 (Sung et al. 2021). Due to the high risk of cancer morbidity and mortality, efforts have been aimed at developing accurate and rapid diagnostic strategies as well as effective therapies for cancer (Li et al. 2017b). Currently, the therapeutic options for cancer include chemotherapy, radiation therapy, and surgery. However, these therapies expose cancer patients to serious side effects and unsatisfactory treatment outcomes (Baumann et al. 2008; Curtin 2012; Leech et al. 2021; Tang et al. 2021). The emerging therapies in cancer treatment, such as immunotherapy (Riley et al. 2019; Zhou et al. 2021), photodynamic therapy (PDT) (Jiang et al. 2019; Li et al. 2020), gene therapy (Rossignoli et al. 2019; Zaimy et al. 2017), and photothermal therapy (PTT) (Liu et al. 2020; Shang et al. 2020), may have the potential for improving cancer treatment outcomes. However, due to tumor heterogeneity and multiple pathways involved in tumor pathogenesis, the efficacies of monotherapy are limited (Conde et al. 2016). For instance, clinical outcomes of many chemotherapeutic drugs are limited by multi-drug resistance (MDR) effects of cancer cells (Chen et al. 2019; Chung et al. 2015). Further, systemic toxicity of chemotherapeutic drugs is a major challenge that should be solved urgently (Chari et al. 2014; Tang et al. 2020b).

Glucose oxidase (GOx) has attracted increasing interest in the biomedical field, especially because of its inherent biocompatibility, non-toxicity, and unique catalysis against β-D-glucose (Fu et al. 2018). It effectively catalyzes glucose oxidation into gluconic acid and hydrogen peroxide (H_2O_2), which can elevate the levels of acidic, hypoxic, and H_2O_2 in the tumor microenvironment (TME). Recently, based on catalytic chemistry of GOx, various multi-modal synergistic cancer therapy strategies have been developed. For example, glucose consumption in combination with starvation and oxidation therapies have been used to treat cancer (Wei et al. 2020). Further, oxygen consumption increases tumor hypoxia, which can be harnessed for hypoxia-activated therapy (Cui et al. 2019; Tang et al. 2020a), whereas increased acidity of the TME can be introduced to trigger sustained drug release from a pH-sensitive drug carrier (Ranji-Burachaloo et al. 2019). Moreover, based on photodynamic therapy (Li et al. 2017a) and/or photothermal therapy (Hu et al. 2019), GOx can interact with photosensitizers or Fenton's reagents to produce multi-modal collaborative cancer treatments. However, studies on GOx-based cancer treatments are in their infancy stages. Therefore, the development and accelerating clinical transformations of GOx-based therapeutic strategies remains a challenge, and the following issues should be addressed by future studies: (i) hypoxia is the most difficult challenge to be overcome during starvation therapy; (ii) the effects of antioxidant stress factors, such as glutathione in tumor cells; (iii) GOx is highly susceptible to degradation after exposure

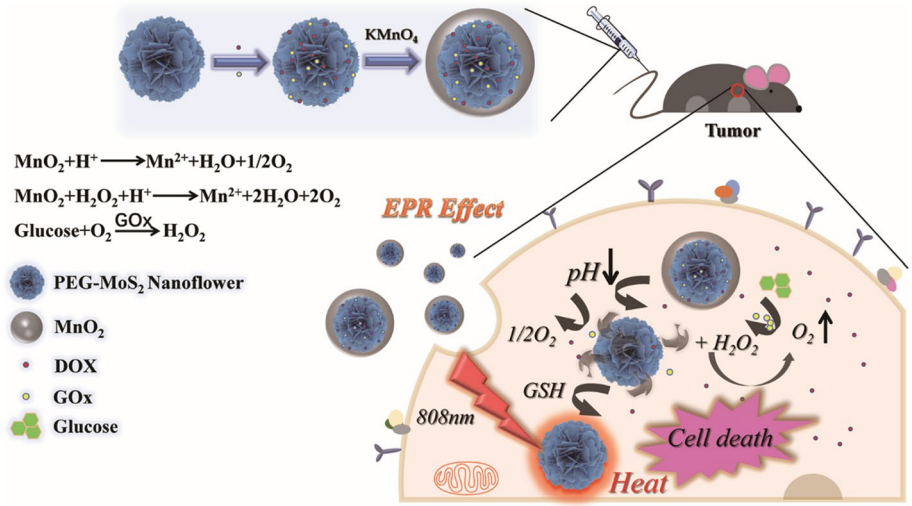

Scheme 1 Synthesis process and treatment schematic of MoS_2@GOx/DOX@MnO_2 nanocatalysts

to biological environments, which is a huge intrinsic drawback for monotherapy (Fu et al. 2018).

In this study, a three-in-one therapy paradigm of tumor starvation/chemical/photothermal therapy is reported (Scheme 1). Polyethylene-glycol-functionalized molybdenum disulfide (PEG-MoS_2) nanoflowers synthesized by a facile one-step preparation as previously reported (Feng et al. 2017; Wu et al. 2019; Yin et al. 2016) were used as carrier substrates for GOx and DOX (M@D/G). The molybdenum disulfide that is currently used for treatment, bioimaging and biosensing applications is usually in 2D form. Although it can also be synthesized with controlled and desired morphologies such as nanosheets, quantum dots, radar-like particles, and nanotubes. However, studies on the synthesis of molybdenum disulfide nanospheres or flower-like particles are few (Yadav et al. 2019). In addition, the synthesis of PEG-MoS_2 nanoflowers can be achieved via the one-step method. Compared to the sheet and tube, the flower shape is conducive for cell phagocytosis and increasing the drug load (Jiang et al. 2020; Sun et al. 2019). This carrier substance was a biologically friendly photothermal agent with high absorption coefficients in the NIR region. The anticancer drugs, DOX and GOx, were loaded into carrier particles via electrostatic interactions (Fernandes et al. 2016, 2019; Zhang et al. 2018a). To prevent premature release of the drug before reaching the tumor site, a manganese dioxide nanoshell was used for encapsulation (M@D/G@M) (Feng et al. 2018). In this strategy, upon internalization of M@D/G@M by cancer cells, the nanosized biocatalyst could be degraded in the acidic TME, thereby releasing the payloads, including GOx, DOX, and Mn^{2+} ions. Then, GOx catalyzed the oxidation of glucose into gluconic acid and H_2O_2, which was accompanied by consumption of O_2. Through a Fenton-like reaction for chemodynamic therapy, elevated H_2O_2 levels were converted into highly toxic ·OH by the released Mn^{2+} ions and thus, the released DOX could further kill the cancer cells. Further, MnO_2 reacted with H_2O_2 and acid to produce O_2, which was provided to the glucose depletion process, thereby forming an effective cycle to promote the glucose consumption rate, leading to starvation treatment. Besides, upon NIR irradiation,

PEG-MoS_2 facilitated GSH oxidation-induced hyperthermia, resulting in a mild temperature increase in the tumor region without the release of toxic metal ions. Such multimodal approaches have the ability to exert stronger therapeutic effects, relative to single therapeutic modes alone.

Materials and methods

Materials and reagents

Glucose oxidase and doxorubicin hydrochloride were obtained from Chengdu Macklin Biochemical Co., Ltd. Sodium molybdate ($Na_2MoO_4{\cdot}2H_2O$), thioacetamide (C_2H_5NS), poly(ethylene glycol), MW: 200 (PEG-200), Poly (allylamine hydrochloride; PAH, 15 kDa), potassium permanganate ($KMnO_4$), potassium sodium tartrate tetrahydrate, trypin, and the cell counting kit-8 (500 T) were acquired from Shanghai Titan Technology Co., Ltd. Dulbecco's modified Eagle's medium (DMEM) and fetal bovine serum were purchased from Chongqing Leger Biotechnology Development Co., Ltd. 3,5-Dinitrosalicylic acid (DNS) and 5,5′-dithiobis (2-nitrobenzoic acid) (DTNB) were obtained from Chongqing Jiaojiao Trading Company. Reactive oxygen species (ROS) fluorescent probe-dihydroethidium (DHE) was purchased from Suzhou Yuheng Biological Technology Co., Ltd. The AO/EB Double Staining Kit was purchased from Sangon Biotech (Shanghai) Co., Ltd. All chemicals were analytical grade and were used as received.

Characterization

Morphologies of the nanocomposites were observed under SEM (Hitachi S4800, Japan). The TEM images were recorded on a JEOL JEM-1200EX (Japanese Electronics and America GATAN). The DLS and Zeta potentials were obtained by NanoBrook Omni particle sizer (Brookhaven Instruments, USA). The XRD pattern was recorded on a D8 ADVANCE diffractometer (Brucker, Germany). The UV–Vis absorption curve was obtained using a UV-2550 Spectrophotometer (Shimadzu, Kyoto, Japan). Fourier transform infrared spectroscopy (FTIR) spectra were collected on a Nicolet IS10 (American Thermoelectric). The XPS were measured using a Thermo Escalab 250Xi (Thermo Scientific Escalab, USA). The TG analysis was performed using a STA 449 F5 Jupiter simultaneous thermal analyzer (Netzsch, Germany).

Synthesis of PEG-MoS_2 nanoflowers

The PEG-MoS_2 nanoflowers were prepared by a facile one-step method. A 5.8 mg sodium molybdate ($Na_2MoO_4{\cdot}2H_2O$) and 6 mg thioacetamide (C_2H_5NS) were dissolved in 10 mL deionized water. Then, ten mL of PEG-200 (1 g mL^{-1}) was added and stirred for 10 min. The resulting suspension was transferred into a polyphenylene-lined stainless steel autoclave and heated at 200 °C for 24 h. After 24 h of chilling at room temperature, the product was washed thrice or more times.

Synthesis of M@D/G@M Nanoparticles

Two mg of DOX was added to 5 mL of synthetic PEG-MoS_2 nanoflower aqueous system and stirred in the dark at 40 °C for 4 h. The resulting material was washed thrice using distilled water and dispersed in 5 mL of distilled water. Further, 5 mg of GOx was added into the MoS_2@DOX (M@D) solution. After 24 h of stirring, M@D/G was obtained

through centrifuging and washing thrice using ddH_2O. Then, M@D/G was dispersed into a $KMnO_4$ solution (0.42 mg/mL). Poly (allylamine hydrochloride) PAH (1 mL, 50 mg/mL) was slowly added and magnetically stirred for 10 min. Finally, M@D/G@M was collected by repeated washing and centrifuging (8000 rpm, 15 min). The encapsulation efficiency of DOX was calculated according to the characteristic peak at 490 nm in the UV–Vis spectroscopy (Fu et al. 2019; Liu et al. 2021; Zhao et al. 2019):

$$\text{Encapsulation efficiency} = ((\text{total}_{\text{DOX}} - \text{unloaded}_{\text{DOX}}) / \text{total}_{\text{DOX}}) \times 100\%.$$

Assessment of photothermal performance and stability in vitro

As previously reported (Wang et al. 2016a, 2016b; Xu et al. 2017), the optimal laser wavelength of molybdenum disulfide material for PTT is 808 nm. Therefore, 808 nm laser (1 W) was used to irradiate different concentrations of PEG-MoS_2 and M@D/G@M. Water was used as the blank control. The change in temperature was recorded using a thermometer. The PEG-MoS_2 aqueous solution was irradiated with a 808 nm laser and naturally cooled to perform the photothermal stability test. Linear time data versus -lnθ were obtained from the cooling period. Then, introduce θ: $\theta = \frac{T-T_0}{T_{\max}-T_0}$, in which T and T_0 are the solution and ambient temperatures of the surrounding, respectively. This procedure was repeated four times and temperature changes recorded. Photothermal conversion efficiencies (η,$\eta = \frac{h\mathrm{A}(\Delta T_{\max,\min} - \Delta T_{\max,H_2O})}{I(1-10^{-\mathrm{A}\lambda})}$) of PEG-$MoS_2$ and M@D/G@M were calculated as previously described (Li et al. 2019; Liu et al. 2013; Ren et al. 2015; Yang et al. 2017). Additional file 1 for specific calculation processes of η are provided in this study.

Catalytic abilities of M@D/G@M

The M@D/G@M (50 μg mL^{-1}) was incubated at room temperature for 4 h with various concentrations of glucose solutions (0–1000 μg mL^{-1}). During the catalytic reaction, changes in H_2O_2 and acidity were, respectively, measured using a H_2O_2 assay kit (Solarbio) and a pH meter (PHS-25 pH tester). The catalytic performance of M@D/G@M on glucose solution (1000 μg mL^{-1}) at different time points was measured within the 4 h.

The detection of glucose consumption

Firstly, the DNS reagent was prepared as previously reported (Zhang et al. 2018b). The glucose concentration was measured according to the standard curve after mixed DNS reagent/glucose samples through a colorimetric reaction process. A certain proportion of nano-biocatalysts dispersed in glucose aqueous solution (0.5 mg mL^{-1}), and then, 0.5 mL of liquid paraffin was added to avoid O_2 exchange from air. After 24 h of incubation, the supernatant to be tested was obtained by centrifuge at 8000 rpm for 15 min. Then, 1 mL of samples, 3 mL of DNS and 1 mL of ultrapure water were mixed with water bath at 100 °C for 5 min. The values of OD_{540} nm of these samples were determined (Ghose 1987):

$$\text{Glucose residue (\%)} = (\text{unreacted}_{\text{Glucose}} / \text{total}_{\text{Glucose}}) \times 100\%.$$

Chemodynamic activities of M@D/G@M

The M@D/G@M (100 μg mL^{-1}), $NaHCO_3$ solution (25 mM), methylene blue (MB) (10 μg mL^{-1}), and H_2O_2 (10 mM) were prepared into a mixture to a total volume of 1 mL. The mixture was shaken at 37 °C under dark conditions for 3 h. When the reaction was over, the supernatant was obtained to measure the remaining MB using a UV/Vis spectrophotometer at 660 nm.

Oxygen production capacity of M@D/G@M

Water, acid, and H_2O_2 were separately added to the M@D/G@M solution. In addition, the appearance of each group of samples was observed. Under different conditions, including M@D/G@M + H_2O_2, M@D/G@M, H_2O_2, glucose, GOx, glucose + GOx, and glucose + M@D/G@M, oxygen concentrations were determined using a dissolved oxygen meter (JPB-607A INESA Scientific Instrument Co., Ltd.).

Ellman's measurement

The PEG-MoS_2 or M@D/G@M (0.5 mg mL^{-1}) and GSH (0.3×10^{-3} mM) were dissolved in 1 mL of a bicarbonate buffer solution. After incubating the reaction system at 37 °C or 45 °C for different time periods, they were equilibrated at room temperature for 3 min. A 200 μL of the Ellman reagent (5,5′-dithiobis (2-nitrobenzoic acid), DTNB; 0.5×10^{-3} M) was then added into the mixture and incubated for 10 min. Finally, the solution was centrifuged at 12,000 rpm for 5 min and the supernatant collected for measurement of absorbance at 410 nm.

Hemolysis assay

A red blood cell (RBC) suspension was prepared as: Anticoagulated venous blood from healthy male BALB/c nude mice (aged 4–5 weeks) was washed using PBS and repeatedly centrifuged at 8000 rpm for 5 min. Upon clarification of the supernatant, 4 times the volume of PBS was added. A 50 μL RBC suspension was mixed with 1 mL M@D/G@M (12.5−400 μg mL^{-1}) in PBS. Further, the same volume of PBS was used as the negative control while water was the positive control. After 1 h, all samples were centrifuged and the supernatants collected for analysis by UV/vis absorbance at 540 nm.

In vitro cytotoxicity

HepG2 cells were seeded in 96-well plates at a density of 5×10^3 per well, incubated for 24 h after which the culture medium was replaced with fresh medium. Subsequently, 10 μL of PEG-MoS_2, M@D@M, M@G@M, and M@D/G@M at different concentrations were added to each well and incubated for 24 h, whereas PBS was used as the control. Cell viabilities were determined using the Cell Counting Kit-8 and calculated as:

$$\text{Cell viability} = (OD_{450}\text{nm of the sample}/OD_{450}\text{nm of the control}) \times 100\%.$$

Survival rate of the cell control group was set to 100%. These assays were performed in triplicate, repeated three times.

Evaluation of cellular glutathione and malondialdehyde (MDA) levels

The HepG2 cells were obtained after being treated with PBS, PEG-MoS_2, M@D/G@M, and M@D/G@M + pH6.0 + NIR in six-well plates. They were lysed and centrifuged at 12,000 rpm for 10 min. The obtained supernatants were used to determine GSH and MDA levels using the Ellman's reagent and MDA kit, respectively.

Live and dead cell staining assay

The HepG2, SMMC7721, and MHCC-97H cells were incubated with PBS, PEG-MoS_2, M@D/G@M, and MDGM + pH6.0 + NIR in six-well plates for 24 h. Five μL of acridine orange (AO) and 5 μL of Ethidium Bromide (EB) staining solutions were added to each group, and gently mixed. After 1–5 min of incubation at room temperature in the dark, cells were observed by an inverted Leica DMI4000 B automatic inverted fluorescence microscope (Additional file 1: Table S1).

Assessment of cellular uptake

The M@D/G@M (50 μg mL^{-1}) was added to HepG2 cells and incubated in a six-well plate. At different time points, the medium was removed, washed using PBS and stained with 4′,6-diamidino-2-phenylindole (DAPI). DOX exhibits a red fluorescence. Endocytosis was observed by Leica TCS SP8 confocal laser scanning microscopy (CLSM). Cells were also obtained for further bioelectron microscopy studies. The parameters that were assessed by fluorescence microscopy are shown in Additional file 1: Table S2.

Intracellular ROS assays

The HepG2 cells were cultured for 24 h at 37 °C in the presence of different materials. Then, the medium was removed and 1 mL of the solution containing the ROS probe (DHE (1 μM)) added to the cells and incubated for 30 min in the dark at 37 °C. The supernatant was removed and the activated DHE fluorescence imaged by Leica DMI4000 B automatic inverted fluorescence microscopy. The fluorescence microscopy parameters were as indicated in Additional file 1: Table S3.

In vivo anti-tumor efficacies

Male BALB/c nude mice (4–5 weeks) were purchased from Chongqing Sishuo Biotechnology Co., Ltd (Chongqing, China). To establish tumor mice models, MHCC-97H cells (10×10^5 cells) were injected into the back of their right shoulders after which mice were randomized into 5 groups ($n = 3$). When tumor volumes reached ≈ 50 mm^3, mice were intravenously treated with PBS + NIR, PEG-MoS_2 + NIR, M@M + NIR, M@D/G@M, and M@D/G@M + NIR (15 mg kg^{-1}). Twenty-four hours after intravenous injections, tumor sites were irradiated twice using 808 nm NIR (1 W) for 5 min at intervals of 10 min.

Body weights and tumor volumes of mice were recorded after every 2 days. Tumor volumes were determined as:

$$\text{Volume} = \left(\text{length} \times \text{width}^2\right)/2.$$

Estimated relative tumor volumes were calculated as:

$\frac{V}{V0}$ ($V0$ represents the tumor volume before treatment).

After 2 weeks of continuous treatment, mice were killed, and solid tumors extracted and photographed. To assess histological changes, the obtained tumors were stained using hematoxylin–eosin (H&E). Major organs (heart, liver, spleen, lungs, and kidneys) for one mouse in each group were collected, fixed in 4% neutral formaldehyde, paraffin-embedded, stained with H&E, and observed to assess in vivo M@D/G@M biocompatibility.

Animal experiments were approved by the Institutional Animal Care and Use Committee of the Animal Experiment Center of Chongqing Medical University (Chongqing, China). Moreover, regulations on management of laboratory animals were adhered to.

Results

Preparation and characterization

Excellent biocompatibilities and solubilities were obtained by introducing polyethylene glycol-200 during the synthesis of the PEG-MoS_2 nanoflower. Morphologies of the nanoflowers are presented in Fig. 1A. Through physical absorption, doxorubicin hydrochloride (DOX) and glucose oxidase (GOx), as well as the natural aerobic dehydrogenase were found to be effectively loaded on the surface of PEG-MOS_2 nanoparticles. The UV–vis spectrum revealed characteristic peaks of DOX and GOx at 490 and 260 nm, respectively, indicating successful loading of these drugs (Fig. 1B). In the presence of cationic polyelectrolyte PAH, the MnO_2 protective shell, which can be used as a pH response, was introduced by reducing $KMNO_4$ and thereby obtaining a multifunctional MnO_2 encapsulated M@D/G therapeutic nanosystem. It was found that the $KMnO_4$ peaks (315, 525, and 545 nm) disappeared, and a new broad peak around 325 nm appeared. This indicated the formation of MnO_2 nanoparticles (Prasad et al. 2014). The new peak at around 325 nm was attributed to the surface plasmon band of colloidal manganese dioxide, which may have been due to the emergence of MnO_2 nanoparticles and red-shifted to a longer wavelength (Luo 2007). It was evident that M@D/G@M did not maintain the nanoflower morphology of PEG-MOS_2, compared to the original sample and hence showed obvious differences upon TEM imaging (Fig. 1C). Furthermore, there were no changes in particle sizes. Dynamic light scattering (DLS) analysis revealed that sizes of PEG-MOS_2 and M@D/G@M in the aqueous solution were 100 and 218.9 nm, respectively (Fig. 1D). This size was larger than the size of the visual electron microscope image, which could be due to Brownian motion of NPs in the solution and includes some solvent layers. Fourier transform infrared spectroscopy (FTIR) confirmed successful loading of DOX and GOx on MoS_2 surfaces and coating of the MnO_2 shell (Fig. 1E). The PEG-MoS_2 curve with typical peaks at 1634 and 2899 cm^{-1} are attributed to C-O and C-H bond vibrations in PEG-MoS_2 (Liu et al. 2014; Yu et al. 2015). Characteristic peaks at 1655 cm^{-1} (C=O vibration in GOx) and 1414 cm^{-1} (C–C vibration in DOX) showed that GOx and DOX were present in M@D/G@M (Fu et al. 2019; Liang et al.

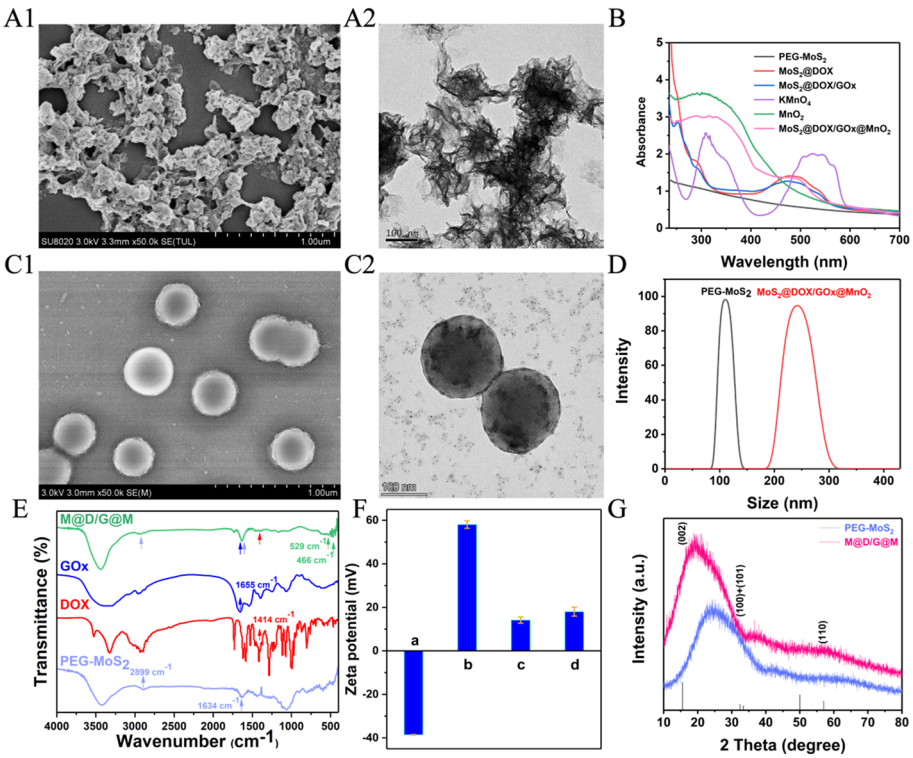

Fig. 1 Property characterization. **A1** SEM, **A2** TEM image of PEG-MoS_2. **B** UV–vis of PEG-MoS_2, MoS_2@DOX, MoS_2@DOX@GOx, $KMnO_4$, MnO_2 and MoS_2@DOX/GOx@MnO_2. **C1** SEM, **C2** TEM image of MoS_2@GOx/DOX@MnO_2, SEM scale bar: 1 μm and TEM scale bar: 100 nm. **D** Hydrated particle size of PEG-MoS_2 and MoS_2@DOX/GOx@MnO_2. **E** FTIR spectra of PEG-MoS_2, DOX, GOx and M@D/G@M. **F** Zeta potential of PEG-MoS_2 (**a**), M@D (**b**), M@D/G (**c**), M@D/G@M (**d**). **G** XRD pattern of PEG-MOS_2 nanoflowers and M@D/G@M. The XRD pattern of MoS_2 showed characteristic peaks at 15.5°, 32.5°,33.3°, and 57.0°, which could be attributed to the (002), (100), (101), and (110) crystal planes of MoS_2 (JCPDS card no. 37-1492). After the MnO_2 shell was coated, it was noted that were no obvious peaks observed in the XRD pattern, indicating that the MnO_2 layer was amorphous

2020). Bands at 529 and 466 cm^{-1} could be attributed to stretching modes of the Mn–O band (Mallakpour et al. 2016). The series change of Zeta potential analysis supports this conclusion (Fig. 1F). The zeta potential of PEG-MoS_2 was measured and found to be − 38.55 ± 0.15395 mV, consistent with previous reports (Wu et al. 2019). The zeta potential value of PEG-MoS_2 was negative, and it became positively charged after DOX loading (58.06 ± 1.71 mV). Moreover, the zeta potential increased from 58.06 ± 1.70614 mV to 14.18 ± 1.45 mV, indicating the encapsulation of GOx. This change may have been because the negative charge of GOx neutralized a part of the positive charge of M@D. The zeta potential of M@D/G@M exhibited a positive charge (18.04 ± 2.08 mV), indicating successful synthesis of manganese dioxide nanoshells (Zhang et al. 2018b). The XRD pattern showed that the chemical structure was PEG-MoS_2, which matched the standard card (JCPDS card No. 37-1492) (Fig. 1G). With regard to the XRD pattern of the M@D/G@M sample, the diffraction peak of PEG-MoS_2 and MnO_2 could be detected, indicating coexistence of the two phases in the sample. Successful synthesis of the material was also confirmed by X-ray photoelectron spectroscopy (XPS) (Additional file 1: Fig. S1). The two peaks in the Mn 2p spectrum were 654.2 eV and 642.4 eV, respectively,

consistent with the Mn (IV) $2p_{2/3}$ and Mn (IV) $2p_{1/2}$ spin–orbit peaks of MnO_2. This confirmed that $KMnO_4$ was converted to MnO_2 by PAH. For quantification of drug loading, the DOX encapsulation ratio was measured by making a standard curve and estimated to be 90.233% (Additional file 1: Fig. S2B). This indicated a high encapsulation efficiency. Thermogravimetric analysis (TGA) of M@D/G@M nanoparticles showed that the loading capacity of GOx was 1.34 wt % (Additional file 1: Fig. S2C).

Photothermal performance of M@D/G@M

After preparation of the nanoparticles, their photothermal properties were evaluated. First, the PEG-MoS_2 showed a strong absorbance from ultraviolet to near-infrared and was not affected by surface PEG modification, implying that it was suitable for PTT applications (Ma et al. 2019). Specifically, under continuous irradiation of the 808 nm laser (1 W), the temperature of PEG-MoS_2 and M@D/G@M increased in a concentration dependent manner. This indicated that PEG-MoS_2 and M@D/G@M could quickly and effectively convert the energy of the NIR laser into heat energy, whereby the maximum temperature reached 50.1 °C and 46.7 °C, respectively (Fig. 2A, B; Additional file 1: Fig. S3). Photothermal conversion efficiencies (η) of PEG-MoS_2 and M@D/G@M were 32.8% and 25.2%, respectively (Fig. 2C, D) (Liu et al. 2013). It was noted that PEG-MoS_2 could be tested well even under four cycles of heating and natural cooling, confirming its high photothermal stability (Fig. 2E). It has been reported that NIR radiation-induced hyperthermia can accelerate glutathione (GSH) depletion in the presence of PEG-MoS_2. Therefore, temperature-dependent GSH oxidation was also investigated. After incubation of GSH with PEG-MoS_2 in water bath for 20 and 120 min, the loss ratio of GSH reached 26.21 ± 0.29% and 77.21 ± 0.028%, respectively (Additional file 1: Fig. S4B).

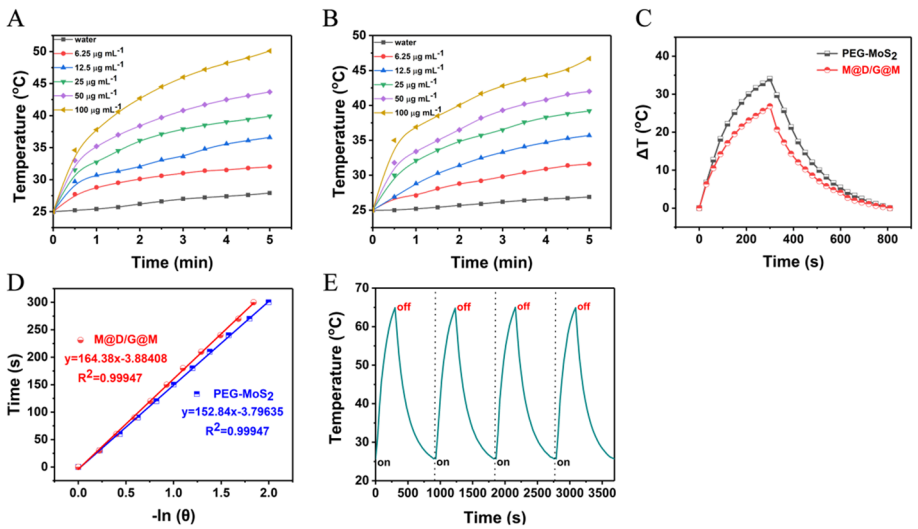

Fig. 2 Photothermal performance. **A** Photothermal temperature curves of PEG-MoS_2 and **B** M@D/G@M dispersed in water at various concentrations of 6.25, 12.5, 25, 50 and 100 μg mL^{-1} under 808-nm laser (1 W) irradiation for 5 min, water as a negative control. **C** Temperature variation curve of PEG-MoS_2 and M@D/G@M under 808 nm laser (1 W) irradiation. **D** Plot of cooling time versus negative natural logarithm of the temperature driving force. The time constants of PEG-MoS_2 and M@D/G@M were calculated to be $\tau_s = 152.84$ s and 164.38 s, respectively. **E** Temperature changes of PEG-MoS_2 aqueous solutions (0.5 mg mL^{-1}) over four ON/OFF cycles of 808 nm laser irradiation (1 W)

However, these were higher than the corresponding results obtained at 37 °C. At 45 °C, the PEG-MoS_2 and M@G/D@M led to GSH depletion, compared to the control and GOx groups (Additional file 1: Fig. S4C). Our findings prove that M@D/G@M nanomaterials are suitable and effective photothermal agents for anti-cancer treatment.

Complement effects of glucose oxidase and manganese dioxide

Manganese dioxide is the most considered choice as an oxygen-generating nanomaterial (Song et al. 2016). In this study, local oxygen concentrations in tumors were increased by the introduction of manganese dioxide nanoshells, with the help of the low pH and high hydrogen peroxide of the tumor microenvironment. Further, pH-responsive manganese dioxide nanoshells were verified by measuring the levels of inclusions, whereby the release of DOX increased with decreasing pH values (Additional file 1: Fig. S2D). Initially, under acidic conditions, the MnO_2 shell of nanoparticles decomposed into Mn^{2+} and O_2 ($MnO_2 + H^+ \rightarrow Mn^{2+} + H_2O + 1/2O_2$), and thus, the contents were released (Feng et al. 2018; Huang et al. 2020). In addition, MnO_2 thoroughly decomposed with increasing acidity and time extension. To evaluate the O_2 generation abilities of MnO_2, the same amount of M@D/G@M solution containing H_2O, acid or H_2O_2, respectively, was prepared (Additional file 1: Fig. S5A). After addition of H_2O_2, there were significant generations of bubbles with the color of the mixture quickly changing from orange-brown to colorless (Mn^{2+}). However, the MnO_2 solution treated with acid or H_2O alone was still brown, and it only became lighter due to double dilution (Additional file 1: Fig. S5B). Further, under different conditions, oxygen concentrations were measured using a dissolved oxygen meter. Oxygen concentrations in the M@D/G@M + H_2O_2 group increased rapidly within 5 min, whereas they were basically unchanged in the M@D/G@M and H_2O_2 solutions, indicating that H_2O_2 was decomposed into oxygen through M@D/G@M (Fig. 3A). In addition, after 10 min of incubation, oxygen concentrations in the glucose + GOx group were markedly reduced from 7.0 mg/L to 0, and this verified that the dissolved oxygen had been depleted by GOx-mediated glucose oxidation (Fig. 3B). That there was no significant drop in the glucose + GOx group could be due to the slow release of GOx in the material. By increasing the reaction temperature, oxygen consumption rates increased, the catalytic process was shortened, which explains the heat promotion effect (Additional file 1: Fig. S5C). The GOx also produces large amounts of H_2O_2 and gluconic acid because it catalyzes glucose in addition to oxygen consumption. Further, catalytic abilities of the nanocomplex can also be assessed by evaluating glucose consumption, hydrogen peroxide production and acidity levels. The measured H_2O_2 levels gradually increased with increasing glucose levels (Fig. 3C), and the increase in acidity was reflected in decreased pH values (Fig. 3D). Similar trends were also noted in the time charts (Fig. 3E, F). Residual glucose concentrations after the reaction were measured using DNS to verify the catalytic potential of the composite material. When the pH was acidic, the MnO_2 nanoshells were dissolved, GOx was released, and glucose was consumed. However, since the liquid paraffin isolated the outside oxygen, glucose could not be further degraded. Only the e group decomposed hydrogen peroxide to generate more oxygen, thereby causing further glucose degradation (Additional file 1: Fig. S6).

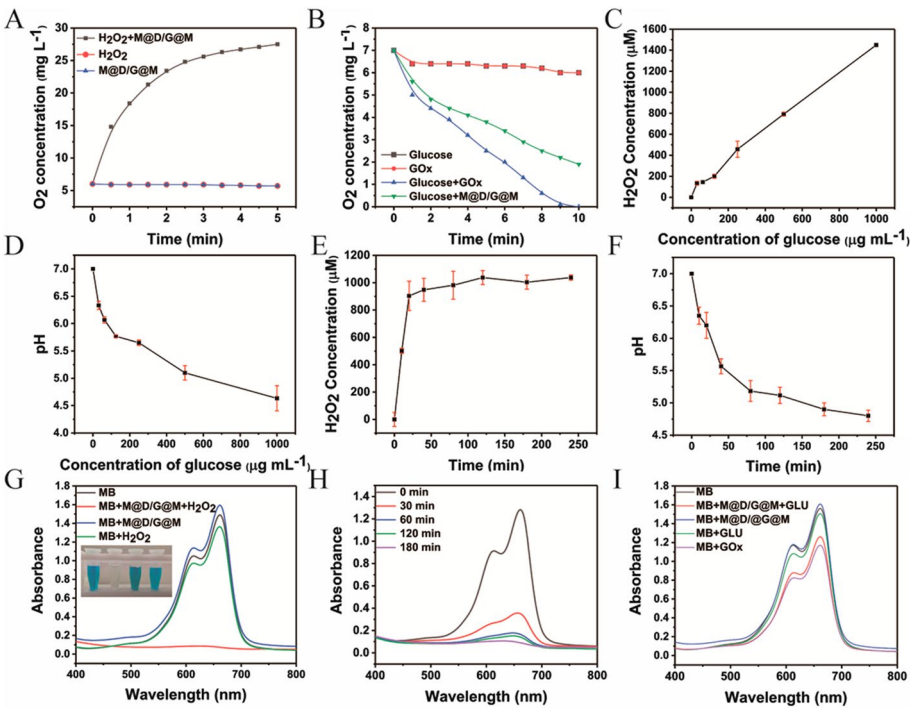

Fig. 3 Catalytic performances. **A** The changes of oxygen concentration in M@D/G@M + H_2O_2, M@D/G@M and H_2O_2 groups. **B** The oxygen concentration changes at different times of GOx-mediated glucose oxidation. **C** The generated H_2O_2 concentration and **D** pH value of the reactions between the M@D/G@M and different concentrations of glucose. **E** Changes of H_2O_2 concentration and **F** pH value caused by the reaction of M@D/G@M and glucose (1 mg mL^{-1}) at different time points. (n = 3, **p < 0.01). **G** UV/vis spectra and photograph (inset) of MB aqueous solution by different treatments for 3 h. **H** MB degraded by M@D/G@M-mediated Fenton-like reaction at different time points. **I** UV/vis spectra of MB aqueous solution treated with M@D/G@M and glucose

The hydroxyl group (·OH) was detected by methylene blue (MB) changes in the system of Mn^{2+}-containing nanomaterials and H_2O_2 through Fenton-like reactions (Shoueir et al. 2018). Therefore, hydroxyl production of M@D/G@M was evaluated with the aid of HCO_3^-, using methylene blue as the indicator. When incubated with M@D/G@M and H_2O_2, MB absorbance was significantly reduced, whereas MB absorbance exhibited a significant change when treated with M@D/G@M or H_2O_2 (Fig. 3G). Degradation of MB was dependent on M@D/G@M and H_2O_2 concentrations (Additional file 1: Fig. S5D–F). The degradation was complete after 3 h, after which absorbance could not be measured (Fig. 3H). The abundant H_2O_2 produced during glucose oxidation by GOx demonstrated that GOx triggered cascade reactions of glucose oxidation and Fenton-like reactions mediated by Mn^{2+}. The MB was partially degraded in the presence of both M@D/G@M and glucose. However, there were no significant changes in degradation of MB when it was acting alone (Fig. 3I). These results indicate that M@D/G@M has a huge potential for enhancing glucose consumption.

Endocytic effects of M@D/G@M and curative effects of multi-therapy

First, the CCK-8 kit was used to verify that the carrier material, PEG-MoS_2 had high biocompatibilities and low cytotoxicities (Fig. 4A, B). Our findings show that PEG-MoS_2

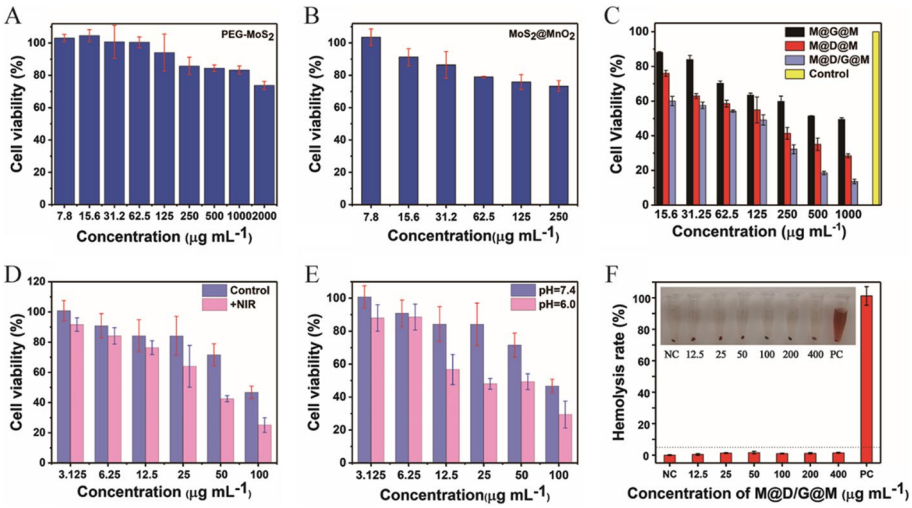

Fig. 4 In vitro cytotoxicity of nanomaterial. Relative viabilities of HepG2 cells after incubation with indicated concentrations of the PEG-MoS_2 (**A**) and MoS_2@MnO_2 (**B**) for 24 h. **C** Relative viabilities of $HepG_2$ cells after incubated with different concentration of M@G@M, M@D@M, M@D/G@M for 24 h. Relative viabilities of $HepG_2$ cells after incubation with indicated concentrations of the M@D/G@M for 24 h with pH7.4 and pH 6.0 (**D**), with/without laser irradiation (1 W) (**E**). **F** Hemolysis of M@D/G@M after incubation with red blood cells at various concentrations for 1 h, using PBS as a negative and deionized water as a positive control, respectively. Error bars were based on three parallel samples

concentrations (from 7.8 μg mL^{-1} to 2 mg mL^{-1}) had high cell viabilities (Fig. 4A). Furthermore, cell viabilities were found to be above 73.3% under treatment of M@M without GOx and DOX loading at 250 μg mL^{-1} (Fig. 4B). Therefore, cell killing effects of either GOx or DOX alone were not as effective as combination therapies (GOx-mediated starvation treatment, Mn^{2+}-mediated CDT, and chemotherapy), which have significant synergistic therapeutic effects (Fig. 4C). The killing effects were further improved by acid response characteristics and photothermal properties of M@D/G@M. Further, conversion of near-infrared light produces thermal damage because low pH can accelerate and promote the release of its contents (Fig. 4D, E). To visually detect the therapeutic effects of M@D/G@M, it was found that after the cells had been treated with AO and EB solutions, live cells could be stained as green fluorescence while dead cells were stained as red fluorescence. Most of the dead cells were observed in the treatment group with pH and near-infrared light (M@D/G@M + pH6.0 + NIR) in various cancer cells (SMMC7721, MHCC-97 and HepG2), compared to the control group (PBS) and the M@D/G@M group (Additional file 1: Fig. S7). The PTT induced by NIR enhanced the tumor cell killing abilities, compared to simply treating cells with M@D/G@M. A hemolysis test was also performed to evaluate the biocompatibility and biosafety of M@D/G@M. Hemolysis rates of 12.5–400 μg mL^{-1} M@D/G@M were lower than 1.6% (Fig. 4F).

Endocytic effects were characterized using CLSM. Red fluorescence of DOX was used to trace the nanoparticles, whereas the DAPI dye was used to label the nucleus. After incubating HepG2 cells with M@D/G@M, fluorescence intensities were captured in a time dependent manner, indicating that M@D/G@M could be effectively internalized into the cytoplasm (Fig. 5). After 4 h of incubation, bioelectron microscopy was

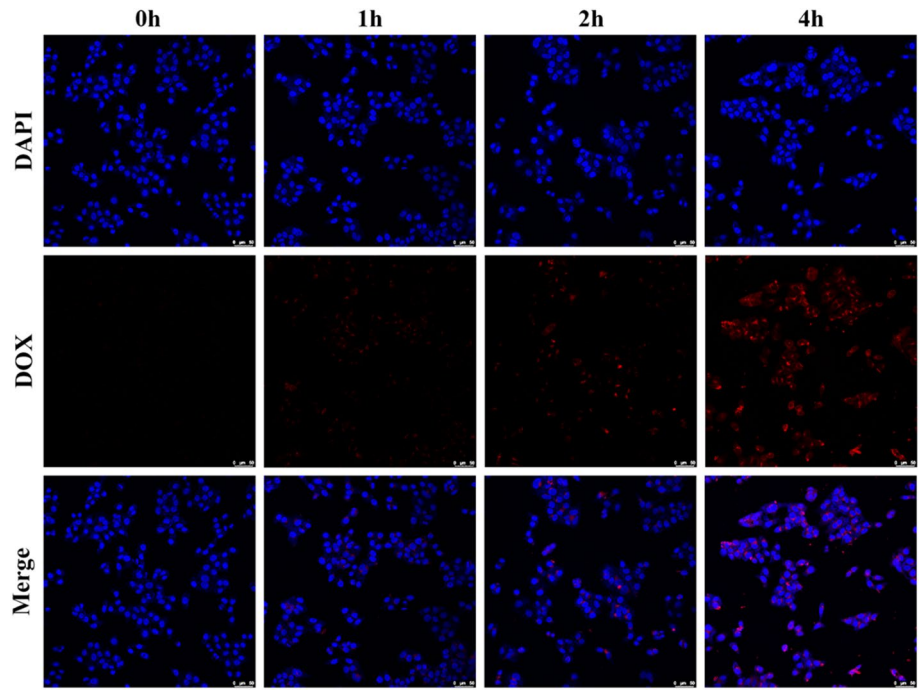

Fig. 5 The uptake of M@D/G@M (50 μg mL^{-1}) under different incubation time. Red and blue colors represent DOX fluorescence and DAPI, respectively. Scale bar: 50 μm

performed, which revealed a large number of M@D/G@M in cytoplasmic vesicles (Additional file 1: Fig. S8).

The significance of M@D/G@M in cancer cells was also investigated. Depletion of intracellular GSH led to redox disorders and increased the intracellular oxidative stress levels. Glutathione levels were significantly suppressed in the M@D/G@M + pH6.0 + NIR group, which facilitated GOx oxidation (Fig. 6A). When MDA reacted with 4,6-dihydroxy-2-mercaptopyrimidine (TBA) under acidic and high temperature conditions, a brown–red substance was produced. The MDA levels can reflect the rates and intensities of lipid peroxidation in cells, which indirectly reflects the degree of tissue peroxidation damage. In this study, MDA levels in the M@D/G@M + pH6.0 + NIR group were significantly high (Fig. 6B), implying a strong degree of peroxidation damage in cells. In addition, fluorescence intensities of ROS in cells treated with M@D/G@M were comparable to the positive control group (H_2O_2 group) (Fig. 6D), which is in agreement with the conclusion that GSH depletion can increase ROS levels and induce oxidative stress. Further, flow cytometry revealed a high apoptosis rate in the M@D/G@M + pH6.0 + NIR group (68.18%), compared to the M@D/G@M group (20.79%) (Fig. 6E). Based on our findings, M@D/G@M increased cell oxidative stress levels to induce cell apoptosis, indicating that M@D/G@M has high cancer treatment potentials.

Anti-tumor efficacies of triple therapy in vivo

In vitro, M@D/G@M exhibited remarkable therapeutic effects. Therefore, anti-cancer efficacies of this nanocomposites were evaluated in mice.

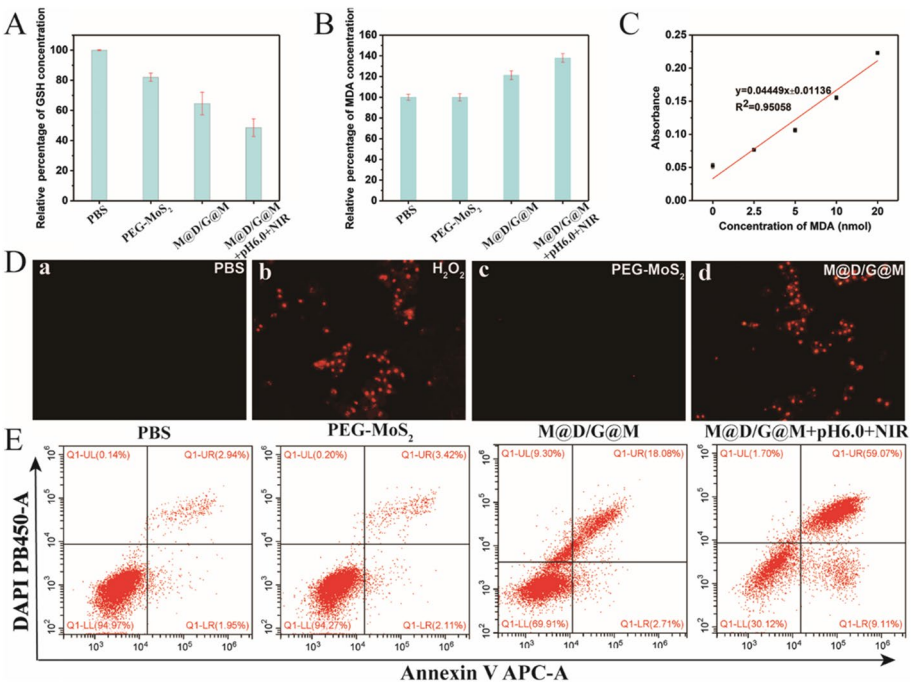

Fig. 6 Investigation of cellular abnormalities and intracellular catalytic mechanism. The concentration of PEG-MoS_2, or M@D/G@M used below is 50 μg mL^{-1}. **A** The relative percentage of intracellular GSH and **B** MDA content. **C** Linear relationship between different concentrations of MDA standards and the absorbance measured by the microplate reader. ($n = 3$, $^{**}p < 0.01$). **D** Generation of ROS after being treated with PBS (**a**), H_2O_2 (**b**), PEG-MoS_2 (**c**), and M@D/G@M (**d**). Scale bar: 50 μm. **E** Apoptosis analyses of HepG2 cells upon 24 h exposure to PBS; PEG-MoS_2, M@D/G@M, M@D/G@M + pH6.0 + NIR groups, respectively

First, MHCC-97H tumor-bearing BALB/c nude mice were randomized into 5 groups and separately treated with PBS + NIR, PEG-MoS_2 + NIR, M@M + NIR, M@D/G@M, and M@D/G@M + NIR. Twenty-four hours after intravenous injection to induce the treatment effects, laser irradiation was performed on mice. To evaluate the photothermal efficacies of M@D/G@M in MHCC-97H tumor-bearing mice, an infrared thermal imager (Fotric 286) was used to record changes in tumor temperature over time. Tumor temperatures in the group treated with molybdenum disulfide component rapidly increased with increasing NIR laser irradiation time (Fig. 7A, C). After 5 min of near-infrared laser irradiation, the maximum temperature reached 44.4 °C, which achieved an effective photothermal treatment outcome. On the contrary, the PBS + NIR group had a temperature increase of less than 1 °C. This phenomenon was attributed to low biological invasiveness of the 808 nm NIR laser and PEG-MoS_2 nanoflowers as well as the M@D/G@M nanocomposites having a strong absorption of 808 nm.

The tumor grew rapidly and uncontrollably when only PEG-MoS_2 + NIR was used for treatment (Fig. 7B, D). The M@D/G@M group showed moderate rates of tumor growth inhibition, which was attributed to tumor starvation effects of GOx and chemotherapy of DOX. In addition, the M@D/G@M + NIR group showed the strongest tumor inhibitory effect, indicating that the efficacy of integrated photothermal therapy was significantly higher than that of pure nanocomposite treatment. Further, after 14 days of various treatments, tumor tissues were analyzed by H&E assays. As shown in Additional

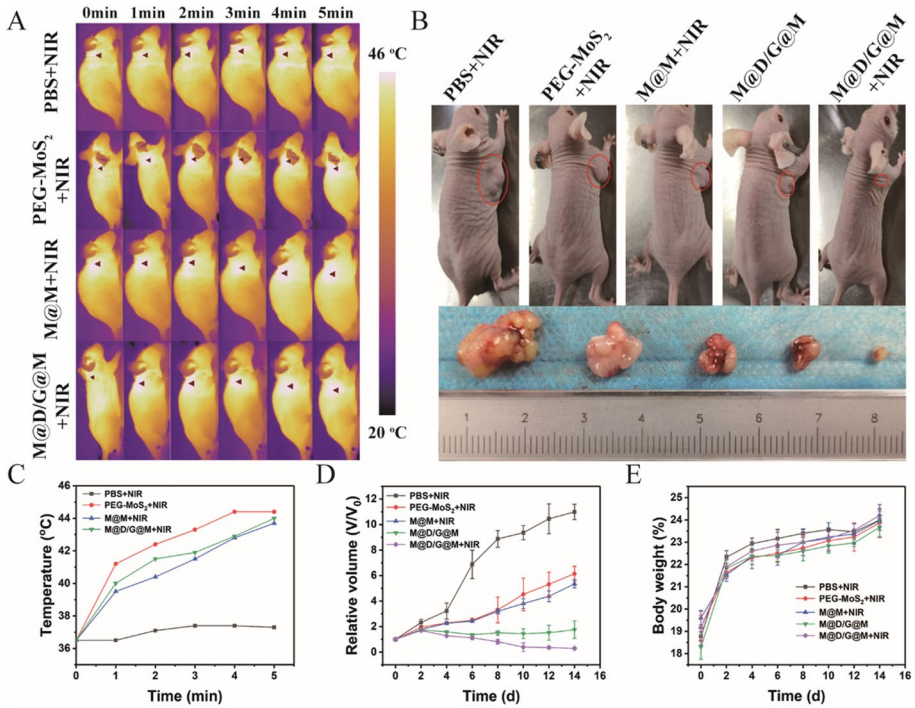

Fig. 7 In vivo anti-tumor assay. **A** IR thermographic images of MHCC-97H tumor-bearing mice in different groups taken under the exposure to an 808 nm laser at a power density of 1 W at different time points. **B** Representative pictures of MHCC-97H tumor-bearing mice and tumor tissues obtained after 14 days of treatment. **C** The temperature change of the corresponding tumor site recorded in **A**. **D** Relative tumor volume in different treatment groups. **E** Mouse body weight recorded every two days

file 1: Fig. S9, the M@D/G@M-treated group with laser irradiation showed obvious extensive damaged areas, compared to other groups.

In addition to therapeutic efficacies of nanosystems, their safety in vivo cannot be ignored. There were no significant differences in final body weights of all five groups of mice, confirming good biocompatibility of the nanosystem (Fig. 7E). The main organs of all tumor-bearing mice were collected on the 14^{th} day to study systemic toxicity and for histological analysis. There were no significant histological damages in major organs (Additional file 1: Fig. S10). Therefore, our findings confirm the in vivo biocompatibility and biosafety of M@D/G@M.

Discussion

Clinically, DOX is widely used in cancer treatment. However, chemotherapy does not always achieve the desired therapeutic effects in cancer patients. The NIR-induced PTT exhibited low toxicity and high treatment specificity, compared to traditional small molecule drugs in tumor chemotherapy (Liu et al. 2015). Even though the efficacy of heating to induce tumor cell death has been assessed, its actual performance is affected by increased heat resistance by tumors after NIR treatment (Kumar et al. 2016; Wang et al. 2016b). Inappropriate light-to-heat conversion materials caused overheating effects of living bodies, leading to serious injuries on non-tumor cells and tissues (Xu et al. 2017). Therefore, there is a need for low temperature-induced photothermal responses to produce a good

therapeutic effect on tumors. Notably, tumor starvation may help eliminate tumor resistance and improve PTT efficacy (Chen et al. 2017). Based on these observations, this study was designed to achieve tumor starvation using GOx as a glucose consumer in the tumor region. Hypoxia in solid tumors can severely limit the catalytic efficiencies of GOx (Rankin et al. 2016). A pH-responsive O_2 self-generated nano-platform using MnO_2-based catalyst-like reaction was developed to overcome this challenge. Through combined applications, the limitations for each method can be avoided and the therapeutic advantages maximized. Our findings show that the nano-platform can effectively inhibit tumor growth and hence act as effective anticancer agents.

Conclusions

An anti-tumor multifunctional nano-platform that combined starvation therapy, chemotherapy, and photothermal therapy was successfully designed. The nanocarrier system was developed around NIR-absorbing polyethylene glycol functionalized molybdenum disulfide nanoflowers. After loading DOX and GOx, manganese dioxide nanoshells were reduced in situ on the surface to increase biocompatibility and prevent leakage of contents. The effects of EPR allowed tumors to accumulate and absorb nanocomposites, whereas the acidic microenvironment of the tumor promoted the release of DOX and GOx, which could directly produce chemotherapy and starvation therapy. Manganese dioxide decomposed H_2O_2 into O_2, overcame the hypoxia of the TME, and promoted the starvation therapeutic effect of the GOx-mediated glucose consumption. Meanwhile, the H_2O_2 from the oxidation of glucose could be used to regenerate O_2 to construct a complementary circulatory system. The role of the external near-infrared light is to stimulate the sensitivity of nanocarriers to photothermal therapy. Further, molybdenum disulfide nanoparticles acted as benign GSH scavengers to enhance cancer treatment. Therefore, this combined treatment system is a potential effective cancer treatment option.

Supplementary Information

The online version contains supplementary material available at https://doi.org/10.1186/s12645-022-00117-y.

Additional file 1. Calculation of the photothermal conversion efficiency, drug loading and releasing behaviors.

Acknowledgements
We would like to express our gratitude to all those who financed this study.

Author contributions
Conceptualization: HT, data curation: KL, SY, ZL, formal analysis: DW, funding acquisition: HT, investigation: KL, SY, methodology: QY, XJ, LC, project administration: HT, resources: ZL, QY, software: KL, LC, supervision: HT, validation: KL, SY, XJ, visualization: HT, writing original draft: KL, writing: review and editing: HT. All authors read and approved the final manuscript.

Funding
This study was supported by the key Laboratory of Infectious Diseases, CQMU (202004) and the Province Natural Science Foundation of Jiangxi Province (20202BABL216040).

Availability of data and materials
Not applicable.

Declarations

Ethics approval and consent to participate
Animal studies in the present study were approved by the Ethics Committee of Animal Experiments of Chongqing Medical University.

Consent for publication
Not applicable.

Competing interests
The authors declare that they have no competing interests. No financial conflict of interest was reported by the authors of this paper.

Author details
[1]Key Laboratory of Molecular Biology for Infectious Diseases (Ministry of Education), Institute for Viral Hepatitis, Department of Infectious Diseases, The Second Affiliated Hospital, Chongqing Medical University, 1 Yi Xue Yuan Road, Chongqing 400016, China. [2]Department of Clinical Laboratory, The First Affiliated Hospital of Nanchang University, Nanchang, Jiangxi, China. [3]Department of Physical Examination, The First Affiliated Hospital of Chongqing Medical University, Chongqing, China. [4]Department of Pathology, The People's Hospital of Rongchang District, Chongqing, China.

Received: 10 October 2021 Accepted: 12 April 2022
Published online: 12 May 2022

References

Baumann M, Krause M, Hill R (2008) Exploring the role of cancer stem cells in radioresistance. Nat Rev Cancer 8(7):545–554
Chari RV, Miller ML, Widdison WC (2014) Antibody-drug conjugates: an emerging concept in cancer therapy. Angew Chem Int Ed Engl 53(15):3796–3827
Chen WH, Luo GF, Lei Q et al (2017) Overcoming the heat endurance of tumor cells by interfering with the anaerobic glycolysis metabolism for improved photothermal therapy. ACS Nano 11(2):1419–1431
Chen W, Shi K, Chu B et al (2019) Mitochondrial surface engineering for multidrug resistance reversal. Nano Lett 19(5):2905–2913
Chung MF, Liu HY, Lin KJ et al (2015) A pH-responsive carrier system that generates no bubbles to trigger drug release and reverse P-glycoprotein-mediated multidrug resistance. Angew Chem Int Ed Engl 54(34):9890–9893
Conde J, Oliva N, Zhang Y et al (2016) Local triple-combination therapy results in tumour regression and prevents recurrence in a colon cancer model. Nat Mater 15(10):1128–1138
Cui D, Huang J, Zhen X et al (2019) A Semiconducting polymer nano-prodrug for hypoxia-activated photodynamic cancer therapy. Angew Chem Int Ed Engl 58(18):5920–5924
Curtin NJ (2012) DNA repair dysregulation from cancer driver to therapeutic target. Nat Rev Cancer 12(12):801–817
Feng H, Tang N, Zhang S et al (2017) Fabrication of layered (CdS-Mn/MoS(2)/CdTe)-promoted TiO(2) nanotube arrays with superior photocatalytic properties. J Colloid Interface Sci 486:58–66
Feng L, Xie R, Wang C et al (2018) Magnetic targeting, tumor microenvironment-responsive intelligent nanocatalysts for enhanced tumor ablation. ACS Nano 12(11):11000–11012
Fernandes DA, Kolios MC (2019) Near-infrared absorbing nanoemulsions as nonlinear ultrasound contrast agents for cancer theranostics. J Mol Liquids 287:110848
Fernandes DA, Fernandes DD, Li Y et al (2016) Synthesis of stable multifunctional perfluorocarbon nanoemulsions for cancer therapy and imaging. Langmuir 32(42):10870–10880
Fu LH, Qi C, Lin J et al (2018) Catalytic chemistry of glucose oxidase in cancer diagnosis and treatment. Chem Soc Rev 47(17):6454–6472
Fu LH, Hu YR, Qi C et al (2019) Biodegradable manganese-doped calcium phosphate nanotheranostics for traceable cascade reaction-enhanced anti-tumor therapy. ACS Nano 13(12):13985–13994
Ghose T (1987) Measurement of cellulase activities. Pure Appl Chem 59(2):257–268
Hu JJ, Liu MD, Gao F et al (2019) Photo-controlled liquid metal nanoparticle-enzyme for starvation/photothermal therapy of tumor by win–win cooperation. Biomaterials 217:119303
Huang J, Huang Y, Xue Z et al (2020) Tumor microenvironment responsive hollow mesoporous Co9S8@MnO2-ICG/DOX intelligent nanoplatform for synergistically enhanced tumor multimodal therapy. Biomaterials 262:120346
Jiang Y, Li J, Zeng Z et al (2019) Organic photodynamic nanoinhibitor for synergistic cancer therapy. Angew Chem Int Ed Engl 58(24):8161–8165
Jiang H, Du Y, Chen L et al (2020) Multimodal theranostics augmented by transmembrane polymer-sealed nano-enzymatic porous MoS2 nanoflowers. Int J Pharm 586:119606
Kumar S, Stokes J 3rd, Singh UP et al (2016) Targeting Hsp70: a possible therapy for cancer. Cancer Lett 374(1):156–166
Leech M, Osman S, Jain S et al (2021) Mini review: personalization of the radiation therapy management of prostate cancer using MRI-based radiomics. Cancer Lett 498:210–216
Li SY, Cheng H, Xie BR et al (2017a) Cancer cell membrane camouflaged cascade bioreactor for cancer targeted starvation and photodynamic therapy. ACS Nano 11(7):7006–7018
Li Z, Tan S, Li S et al (2017b) Cancer drug delivery in the nano era: an overview and perspectives (Review). Oncol Rep 38(2):611–624
Li X, Jiang M, Zeng S et al (2019) Polydopamine coated multifunctional lanthanide theranostic agent for vascular malformation and tumor vessel imaging beyond 1500 nm and imaging-guided photothermal therapy. Theranostics 9(13):3866–3878
Li X, Lovell JF, Yoon J et al (2020) Clinical development and potential of photothermal and photodynamic therapies for cancer. Nat Rev Clin Oncol 17(11):657–674
Liang J, Yang X, Liu D et al (2020) Lipid/hyaluronic acid-coated doxorubicin-Fe_3O_4 as a dual-targeting nanoparticle for enhanced cancer therapy. AAPS PharmSciTech 21(6):235
Liu Y, Ai K, Liu J et al (2013) Dopamine-melanin colloidal nanospheres: an efficient near-infrared photothermal therapeutic agent for in vivo cancer therapy. Adv Mater 25(9):1353–1359
Liu T, Wang C, Gu X et al (2014) Drug delivery with PEGylated MoS2 nano-sheets for combined photothermal and chemotherapy of cancer. Adv Mater 26(21):3433–3440

Liu Z, Liu J, Wang R et al (2015) An efficient nano-based theranostic system for multi-modal imaging-guided photothermal sterilization in gastrointestinal tract. Biomaterials 56:206–218
Liu S, Pan X, Liu H (2020) Two-dimensional nanomaterials for photothermal therapy. Angew Chem Int Ed Engl 59(15):5890–5900
Liu M, Ma W, Zhao D et al (2021) Enhanced penetrability of a tetrahedral framework nucleic acid by modification with iRGD for DOX-targeted delivery to triple-negative breast cancer. ACS Appl Mater Interfaces 13(22):25825–25835
Luo Y (2007) Preparation of MnO_2 nanoparticles by directly mixing potassium permanganate and polyelectrolyte aqueous solutions. Mater Lett 61(8–9):1893–1895
Ma M, Liu X, Tan L et al (2019) Enhancing the antibacterial efficacy of low-dose gentamicin with 5 minute assistance of photothermy at 50 °C. Biomater Sci 7(4):1437–1447
Mallakpour S, Madani M (2016) Functionalized-MnO_2/chitosan nanocomposites: a promising adsorbent for the removal of lead ions. Carbohydr Polym 147:53–59
Prasad P, Gordijo CR, Abbasi AZ et al (2014) Multifunctional albumin-MnO_2 nanoparticles modulate solid tumor microenvironment by attenuating hypoxia, acidosis, vascular endothelial growth factor and enhance radiation response. ACS Nano 8(4):3202–3212
Ranji-Burachaloo H, Reyhani A, Gurr PA et al (2019) Combined Fenton and starvation therapies using hemoglobin and glucose oxidase. Nanoscale 11(12):5705–5716
Rankin EB, Giaccia AJ (2016) Hypoxic control of metastasis. Science 352(6282):175–180
Ren W, Yan Y, Zeng L et al (2015) A near infrared light triggered hydrogenated black TiO_2 for cancer photothermal therapy. Adv Healthc Mater 4(10):1526–1536
Riley RS, June CH, Langer R et al (2019) Delivery technologies for cancer immunotherapy. Nat Rev Drug Discov 18(3):175–196
Rossignoli F, Grisendi G, Spano C et al (2019) Inducible Caspase9-mediated suicide gene for MSC-based cancer gene therapy. Cancer Gene Ther 26(1–2):11–16
Shang T, Yu X, Han S et al (2020) Nanomedicine-based tumor photothermal therapy synergized immunotherapy. Biomater Sci 8(19):5241–5259
Shoueir K, El-Sheshtawy H, Misbah M et al (2018) Fenton-like nanocatalyst for photodegradation of methylene blue under visible light activated by hybrid green DNSA@Chitosan@MnFe(2)O(4). Carbohydr Polym 197:17–28
Song M, Liu T, Shi C et al (2016) Bioconjugated manganese dioxide nanoparticles enhance chemotherapy response by priming tumor-associated macrophages toward M1-like phenotype and attenuating tumor hypoxia. ACS Nano 10(1):633–647
Sun G, Yang S, Cai H et al (2019) Molybdenum disulfide nanoflowers mediated anti-inflammation macrophage modulation for spinal cord injury treatment. J Colloid Interface Sci 549:50–62
Sung H, Ferlay J, Siegel RL et al (2021) Global Cancer Statistics 2020: GLOBOCAN estimates of incidence and mortality worldwide for 36 cancers in 185 countries. CA Cancer J Clin 71(3):209–249
Tang Y, Ji Y, Yi C et al (2020a) Self-accelerating H(2)O(2)-responsive plasmonic nanovesicles for synergistic chemo/starving therapy of tumors. Theranostics 10(19):8691–8704
Tang Y, Liu H, Chen H et al (2020b) Advances in aptamer screening and drug delivery. J Biomed Nanotechnol 16(6):763–788
Tang N, Li H, Zhang L et al (2021) A macromolecular drug for cancer therapy via extracellular calcification. Angew Chem Int Ed Engl 60(12):6509–6517
Wang J, Tan X, Pang X et al (2016a) MoS2 quantum Dot@Polyaniline inorganic-organic nanohybrids for in vivo dual-modal imaging guided synergistic photothermal/radiation therapy. ACS Appl Mater Interfaces 8(37):24331–24338
Wang S, Tian Y, Tian W et al (2016b) Selectively sensitizing malignant cells to photothermal therapy using a CD44-targeting heat shock protein 72 depletion nanosystem. ACS Nano 10(9):8578–8590
Wei C, Liu Y, Zhu X et al (2020) Iridium/ruthenium nanozyme reactors with cascade catalytic ability for synergistic oxidation therapy and starvation therapy in the treatment of breast cancer. Biomaterials 238:119848
Wu S, Liu X, Ren J et al (2019) Glutathione depletion in a benign manner by MoS2-based nanoflowers for enhanced hypoxia-irrelevant free-radical-based cancer therapy. Small 15(51):e1904870
Xu J, Gulzar A, Liu Y et al (2017) Integration of IR-808 sensitized upconversion nanostructure and MoS2 nanosheet for 808 nm NIR light triggered phototherapy and bioimaging. Small 13(36):1701841
Yadav V, Roy S, Singh P et al (2019) 2D MoS(2)-based nanomaterials for therapeutic, bioimaging, and biosensing applications. Small 15(1):e1803706
Yang G, Xu L, Chao Y et al (2017) Hollow MnO(2) as a tumor-microenvironment-responsive biodegradable nano-platform for combination therapy favoring antitumor immune responses. Nat Commun 8(1):902
Yin W, Yu J, Lv F et al (2016) Functionalized nano-MoS(2) with peroxidase catalytic and near-infrared photothermal activities for safe and synergetic wound antibacterial applications. ACS Nano 10(12):11000–11011
Yu J, Yin W, Zheng X et al (2015) Smart MoS_2/Fe_3O_4 nanotheranostic for magnetically targeted photothermal therapy guided by magnetic resonance/photoacoustic imaging. Theranostics 5(9):931–945
Zaimy MA, Saffarzadeh N, Mohammadi A et al (2017) New methods in the diagnosis of cancer and gene therapy of cancer based on nanoparticles. Cancer Gene Ther 24(6):233–243
Zhang MK, Li CX, Wang SB et al (2018a) Tumor starvation induced spatiotemporal control over chemotherapy for synergistic therapy. Small 14(50):e1803602
Zhang YH, Qiu WX, Zhang M et al (2018b) MnO2 motor: a prospective cancer-starving therapy promoter. ACS Appl Mater Interfaces 10(17):15030–15039
Zhao J, Li X, Wang X et al (2019) Fabrication of hybrid nanostructures based on Fe(3)O(4) nanoclusters as theranostic agents for magnetic resonance imaging and drug delivery. Nanoscale Res Lett 14(1):200
Zhou W, Zhou Y, Chen X et al (2021) Pancreatic cancer-targeting exosomes for enhancing immunotherapy and reprogramming tumor microenvironment. Biomaterials 268:120546

Publisher's Note